Formation of $Zn_{1-x}Mn_xS$ Nanowires within Mesoporous Silica of Different Pore Sizes

Felix J. Brieler,[2] Petra Grundmann,[2] Michael Fröba,*[,2] Limei Chen,[3] Peter J. Klar,*[,3] Wolfram Heimbrodt,[3] Hans-Albrecht Krug von Nidda,[§] Thomas Kurz,[§] and Alois Loidl[§]

Contribution from the Institute of Inorganic and Analytical Chemistry, Justus-Liebig University Giessen, Heinrich-Buff-Ring 58, 35392 Giessen, Germany, Department of Physics and Material Sciences Center, Philipps University of Marburg, Renthof 5, 35032 Marburg, Germany, and Experimental Physics V, Electronic Correlations and Magnetism, Institute of Physics, University of Augsburg, Universitätsstrasse 2, 86135 Augsburg, Germany

Abstract: Arrays of highly ordered $Zn_{1-x}Mn_xS$ quantum wires with x ranging from 0.01 to 0.3 and with lateral dimensions of 3, 6, and 9 nm were synthesized within mesoporous SiO_2 host structures of the MCM-41 and SBA-15 type. The hexagonal symmetry of these arrays (space group $p6m$) and the high degree of order was confirmed by X-ray diffraction and transmission electron microscopy (TEM) studies. Physisorption measurements show the progressive filling of the pores of the SiO_2 host structures, while TEM and Raman studies reveal the wire-like character of the incorporated $Zn_{1-x}Mn_xS$ nanostructures. X-ray absorption near-edge structure, extended X-ray absorption fine structure, photoluminescence excitation (PLE), and electron paramagnetic resonance studies confirm the good crystalline quality of the incorporated $Zn_{1-x}Mn_xS$ guest species and, in particular, that the Mn^{2+} ions are randomly distributed and are situated on tetrahedrally coordinated cation sites of the $Zn_{1-x}Mn_xS$ wires for all x up to 0.3. The amount of Mn^{2+} ions loosely bound to the surface of the $Zn_{1-x}Mn_xS$ nanowires is less than 4% of the total Mn content even for the 3 nm nanostructures up to the highest Mn content of $x = 0.3$. The effects of the reduction of the lateral dimensions on electronic properties of the diluted magnetic semiconductor were studied by PLE spectroscopy. Due to the quantum confinement of the excitons in the wires an increase of the direct band gap with decreasing particle size is observed.

Introduction

Rare-earth- and transition-metal-doped II−VI semiconductors and semiconductor nanostructures are currently of interest because of their optical and magnetic properties.[1]

ZnS:Mn has been employed as active material in electroluminescent devices for decades.[2−4] Many attempts were carried out in order to dope this semiconductor with different transition-metal ions whereby intense visible-light emissions with different colors were achieved.[5,6] In 1994 it was proposed by Bhargava et al. that nanocrystals of ZnS:Mn show a high-luminescence quantum efficiency and lifetime shortening of the Mn internal transitions.[7] Further studies suggested that the latter effect is not necessarily a nanosize effect, and an effective lifetime shortening of the Mn internal transitions might also arise from competing recombination paths due to defects in the nanoparticles.[8] Due to the large surface-to-volume ratio in nanoparticles defect formation as well as Mn diffusion to the surface can have a significant influence on the optical properties and will strongly depend on the synthesis procedure.[9,10]

Magnetic semiconductors and semiconductor nanostructures are possible candidates for spin aligners and spin injectors in future spintronic devices.[11] The family of $A_{1-x}Mn_xB$ (where A and B are group II and VI elements, respectively) are a subgroup of the so-called diluted magnetic semiconductors (DMS). These DMS have gained considerable interest due to their unusual magnetooptical properties. It is strongly anticipated that the reduction of the lateral dimensions of magnetic semiconductor nanostructures will also significantly affect their magnetic properties.[1] An understanding of the magnetism at reduced

[2] Justus-Liebig University Giessen.
[3] Philipps University of Marburg.
[§] University of Augsburg.

(1) Heimbrodt, W.; Klar, P. J. Magnetic Semiconductor Nanostructures. In *Magnetic Nanostructures*; Nalwa, H. S., Ed.; American Scientific Publishers: Stevenson Ranch, CA, 2002.
(2) Mach, R.; Müller, G. O.*Phys. Status Solidi A* **1984**, *81*, 609.
(3) Falcony, C.; Garcia, M.; Ortiz A.; Alonso, J. C. *J. Appl. Phys.* **1992**, *72*, 1525.
(4) Krasnov, A. N. *Appl. Phys. Lett.* **2001**, *78*, 3223.
(5) Yang, P.; Lu, M. K.; Zhou, G. J.; Yuan, D. R.; Xu, D. *Inorg. Chem. Commun*. **2001**, *4*, 734.
(6) Yang, P.; Lu, M.; Xu, D.; Yuan, D.; Zhou, G. *Appl. Phys. A* **2001**, *73*, 455.
(7) Bhargava, R. N.; Gallagher, D.; Hong, X.; Nurmikko, A. *Phys. Rev. Lett.* **1994**, *72*, 416.
(8) Bol, A. A.; Meijerink, A. *Phys. Rev. B: Condens. Matter Mater. Phys.* **1998**, *58*, R15997.
(9) Igarashi, T.; Isobe, T.; Senna, M. *Phys. Rev. B: Condens. Matter Mater. Phys.* **1997**, *56*, 6444.
(10) Borse, P. H.; Srinivas, D.; Shinde, R. F.; Date, S. K.; Vogel, W.; Kulkarni, S. K. *Phys. Rev. B: Condens. Matter Mater. Phys.* **1999**, *60*, 8659.
(11) Special Issue: Semiconductor Spintronics; Ohno, H., Ed. *Semicond. Sci. Technol.* **2002**, *17*, 275.

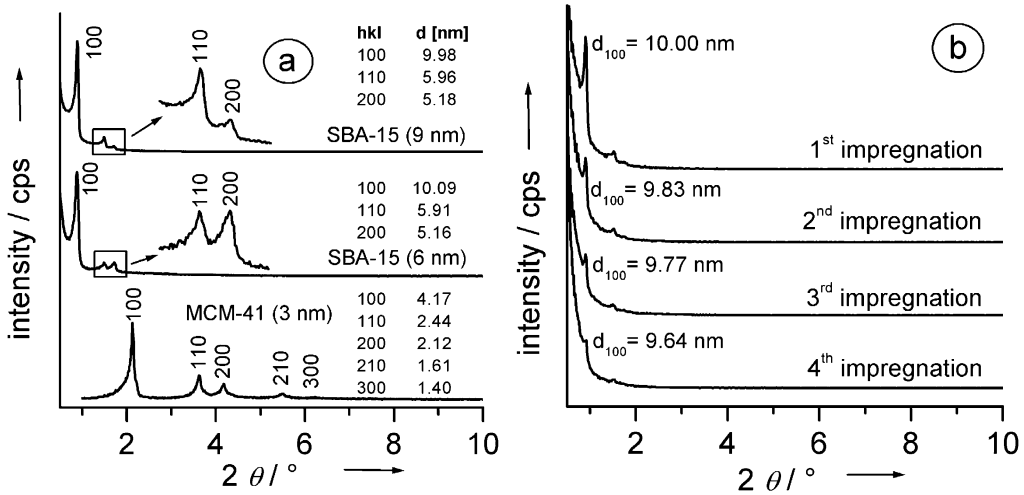

Figure 1. (a) P-XRD of mesoporous silica with three different pore diameters: MCM-41 (3 nm) and SBA-15 (6 and 9 nm). (b) P-XRD of $Zn_{0.8}Mn_{0.2}S$@SBA-15 (9 nm) after the four different impregnation/conversion cycles.

dimensions is essential for device miniaturization. The magnetic properties of a $A_{1-x}Mn_xB$ nanoparticle will — similar to the optical properties — strongly depend on the Mn distribution within the nanoparticle and thus on the synthesis procedure.[12]

The most common method for the synthesis of DMS nanoparticles is the utilization of water-in-oil droplets, which serve as a size-limiting minireactor.[13] Mesoporous materials, first introduced in 1992,[14] have opened new pathways for the formation of nanostructured host/guest compounds.[15] At first highly ordered mesoporous materials with pore sizes of about 3 nm were accessible through the M41S family with either hexagonal (so-called MCM-41) or cubic symmetry (MCM-48).[14] By using different amphiphilic structure directing agents such as triblock copolymers (Pluronics) hexagonally ordered mesoporous materials containing large pores with diameters up to 10 nm or more could be synthesized (so-called SBA-15).[16] Fine-tuning the pore size of SBA-15 from 5 to 30 nm is possible just by varying the synthesis temperature.[17]

The hexagonal order of MCM-41 and SBA-15 provides the possibility of growing quantum wires inside the channels.[18] The incorporation of semiconductors into the pores seems promising, because the silica-wall structure of the host materials with its large band gap serves as a barrier between single wires. Several semiconductor compounds, such as CdS,[19,20] (Cd,Mn)S,[18,21,22] CdSe,[23] (Cd,Mn)Se,[24] ZnS,[25](Zn,Mn)S,[26] GaAs,[27] InP,[28] Ge,[29] and SiGe[30] have been implanted into MCM-41 or SBA-15 so far to obtain regular arrays of quantum wires.

Recently we reported on the successful incorporation of the DMS compound $Cd_{1-x}Mn_xS$ into the pore system of MCM-41 silica.[22] In contrast to other approaches it was possible to synthesize the semiconductor inside the channels without preceding functionalization of the inner surface with thiol groups.[20,25] Powder X-ray diffraction (P-XRD), electron microscopy, and physisorption measurements clearly showed the preservation of the mesoscopic order. Optical measurements proved the intrapore formation of crystalline $Cd_{1-x}Mn_xS$ particles. Raman as well as electron paramagnetic resonance (EPR) results suggested an almost random distribution of the Mn ions within the nanocluster and no indication for a strong enhancement of the Mn content at the surface of the nanoparticles. A blue shift of the band-gap energy of about 200 meV due to quantum confinement was observed.

Here we report on the incorporation of $Zn_{1-x}Mn_xS$ with different doping levels x (from 0.01 to 0.3) inside three different SiO_2 pore systems with pore diameters of 3 nm (MCM-41) and 6 and 9 nm (both SBA-15). We will discuss in detail the pore structure of the mesoporus SiO_2 hosts before and after the intrapore synthesis of the $Zn_{1-x}Mn_xS$ nanoparticles. We will also assess the nanoscopic structure of the $Zn_{1-x}Mn_xS$ guest nanoparticles as a function of Mn content with special emphasis on the Mn sites. Finally, we report on the effect of the reduced dimensions on the electronic and vibrational properties of these $Zn_{1-x}Mn_xS$ wire systems of different wire diameters.

Results and Discussion

Powder X-ray Diffraction. The powder X-ray diffraction patterns of the pristine calcined or extracted silica phases clearly demonstrate the hexagonal symmetry of the space group *p6m* (Figure 1a). The similarity in the *d* spacing of SBA-15 with 6

(12) Tsujii, N.; Kitazawa, H.; Kido, G. *J. Appl. Phys.* **2003**, *93*, 6957.
(13) Pileni, M. *Catal. Today* **2000**, *58*, 151.
(14) Kresge, C. T.; Leonowicz, M. E.; Roth, W. J.; Vartulli, J. C.; Beck, J. S. *Nature* **1992**, *359*, 710.
(15) Möller, K.; Bein, T.*Chem. Mater.* **1998**, *10*, 2950.
(16) Zhao, D.; Huo, Q.; Feng, J.; Chmelka, B. F.; Stucky, G. D. *J. Am. Chem. Soc.* **1998**, *120*, 6024.
(17) Zhao, D.; Feng, J.; Huo, Q.; Melosh, N.; Fredrickson, G. H.; Chmelka, B. F.; Stucky, G. D. *Science* **1998**, *279*, 548.
(18) Chen, L.; Klar, P. J.; Heimbrodt, W.; Brieler, F.; Fröba, M.*Appl. Phys. Lett.* **2000**, *76*, 3531.
(19) Hirai, T.; Okubo, H.; Komasawa, I. *J. Phys. Chem. B* **1999**, *103*, 4228.
(20) Xu, W.; Liao, Y.; Akins, D. L. *J. Phys. Chem. B* **2002**, *106*, 11127.
(21) Chen, L.; Falk, H.; Klar, P. J.; Heimbrodt, W.; Brieler, F.; Fröba, M.; Krug von Nidda, H.-A.; Loidl, A.; Chen; Z.; Oka, Y. *Phys. Status Solidi B* **2002**, *229*, 31.
(22) Brieler, F. J.; Fröba, M.; Chen, L.; Klar, P. J.; Heimbrodt, W.*Chem. Eur. J.* **2002**, *8*, 185.
(23) Parala, H.; Winkler, H.; Kolbe, M.; Wohlfahrt, A.; Fischer, R. A.; Schmechel, R.; von Seggern, H. *Adv. Mater.* **2000**, *12*, 1050.
(24) Chen, L.; Klar, P. J.; Heimbrodt, W.; Brieler, F.; Fröba, M.; Krug von Nidda, H.-A.; Loidl, A. *Physica E* **2001**, *10*, 368.
(25) Zhang, W.-H.; Shi, J.-L.; Chen, H.-R.; Hua, Z.-L.; Yan, D. S. *Chem. Mater.* **2001**, *13*, 684.
(26) Chen, L.; Klar, P. J.; Heimbrodt, W.; Brieler, F.; Fröba, M.; Krug von Nidda, H.-A.; Kurz, T.; Loidl, A. *J. Appl. Phys.* **2003**, *93*, 1326.
(27) Srdanov, V. I.; Alxneit, I.; Stucky, G. D.; Reaves, C. M.; DenBaars, S. P. *J. Phys. Chem. B* **1998**, *102*, 3341.
(28) Agger, J. R.; Anderson, M. W.; Pemble, M. E.; Terasaki, O.; Nozue, Y. *J. Phys. Chem. B* **1998**, *102*, 3345.
(29) Leon, R.; Margolese, D.; Stucky, G.; Petroff, P. M. *Phys. Rev. B* **1995**, *52*, R2285.
(30) Tang, Y. S.; Cai, S.; Jin, G.; Duan, J.; Wang, K. L.; Soyez, H. M.; Dunn, B. S. *Appl. Phys. Lett.* **1997**, *71*, 2449.

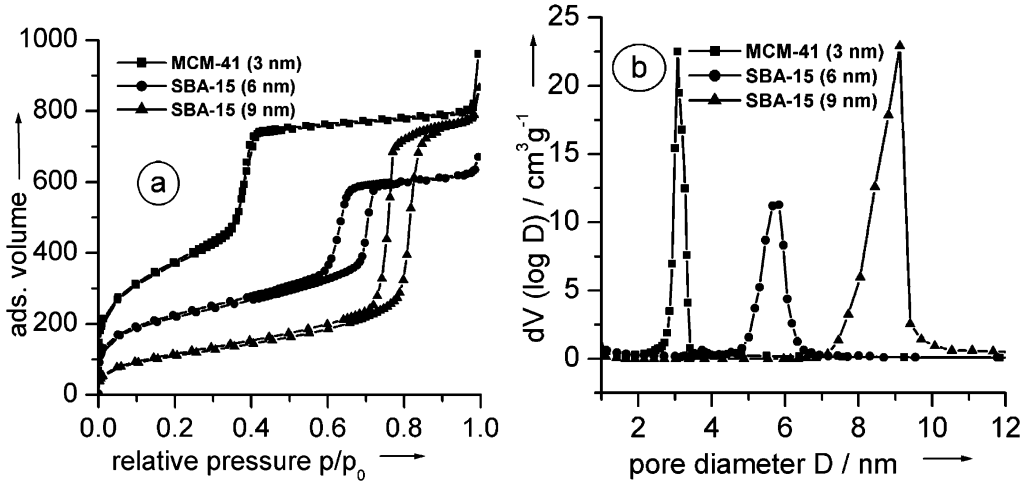

Figure 2. Nitrogen adsorption/desorption isotherms (a) and BJH pore-size distributions (b) of the three mesoporous host structures.

and 9 nm pore diameter is due to a different wall thickness. Whereas SBA-15 with 6 nm pore diameter has a wall thickness of approximately 5.6 nm, SBA-15 with 9 nm pore diameter only has a wall thickness of 2.5 nm, thus resulting in a very similar *d* spacing. A high degree of long-range order can be assumed according to the reflections at higher scattering angles 2θ for all mesoporous host structures.

After the intrapore formation of the DMS compound (in this case $Zn_{0.8}Mn_{0.2}S$, Figure 1b) the XRD peaks are reduced in intensity and slightly shifted to smaller *d* spacings, proving the conservation of the mesoporous host. The intensity of the Bragg reflections originates from the difference in the scattering power between the silica walls and the empty pores. Due to the impregnation of the pores with scattering material, the amount of scattering power within the pores is increased, resulting in an overall loss of intensity due to phase cancellation between the pore walls and the guest species. This is a well-known phenomenon in the literature.[22,31,32]

In the 2θ region between 20 and 60° no reflections of the bulk DMS compounds are present. The observed features are the same in all three different host structures for all incorporated samples $Zn_{1-x}Mn_xS$. From the XRD measurements it can be concluded that the formation of the guest species has taken place preferentially inside the pore system of the respective host material and no bulk material has been formed.

Nitrogen Physisorption. In Figure 2 the nitrogen physisorption isotherms and the pore-size distribution of the three host structures are displayed. All three structures show a type IV isotherm, typical for mesoporous materials.[33] A H1 hysteresis loop is only observed for the SBA-15 host structures. This is due to the fact, that the occurrence of sorption hysteresis depends on temperature, pore size, and shape, i.e. the thermodynamic states of pore fluid and bulk fluid.[34] Thus, materials with cylindrical pores < 4 nm do not show a hysteresis loop. The pore sizes were calculated from the desorption branch of the isotherms using the Barrett−Joyner−Halenda (BJH) formula,[35] despite the fact, that this well-established theory is actually valid only for materials with pores > 4 nm and underestimates the diameter of mesopores (with pore diameters < 4 nm) by approximately 1 nm.[36,37] However, it is an appropriate method for determining changes in the pore-size distributions. More detailed and accurate calculations could be achieved using the relatively new method of determining the pore sizes with the non-local density functional theory (NLDFT).[38] This model is so far only valid for pure porous structures, such as porous silicas or carbons, and not for host/guest systems, so for comparison reasons for all samples the BJH-algorithm was used.

In Figure 3 the isotherms for $Zn_{0.9}Mn_{0.1}S$@SBA-15 (6 nm) after the respective impregnation/conversion cycles and the pristine SBA-15 together with the Brunauer−Emmett−Teller (BET) surface area are shown. After the intrapore formation of the DMS compounds no change in the isotherm type is observed, proving the conservation of the cylindrical pore system, whereas the change from H1 to H2 hysteresis indicates a partial filling of the pores. The amount of adsorbed nitrogen as well as the BET surface area is strongly reduced with increasing pore filling, i.e. the number of impregnation/conversion cycles, but still mesoporosity can be found, which again proves the preservation of the mesoporous host structure and leads to the conclusion that particles are formed inside the pores.

The mean pore diameter (Figure 3b) is decreasing as indicated by the shift of the main peak of the pore-size distribution to smaller values. Also the amount of adsorbed nitrogen is strongly decreasing. All these results clearly demonstrate a coating of the walls of the pores and a progressing slow filling with the guest species. The total pore volume calculated at $p/p_0 = 0.9$ is 0.87 cm^3/g for the pristine SBA-15 and 0.27 cm^3/g for the host/guest compound after the third impregnation/conversion cycle. This indicates a degree of filling of the pores of over 65%.

The observed effects are very similar for all intrapore formations inside the different host structures and are known in the literature for similar host/guest systems.[39]

Transmission Electron Microscopy. The results of the XRD and nitrogen physisorption experiments are substantiated by

(31) Hammond, W.; Prouzet, E.; Mahanti, S. D.; Pinnavaia, T. J. *Microporous Mesoporous Mater.* **1999**, *27*, 19.
(32) Fröba, M.; Köhn, R.; Bouffaud, G.*Chem. Mater.* **1999**, *11*, 2858.
(33) IUPAC Manual of Symbols and Terminology, Appendix 2, Part 1. *Pure Appl. Chem.* **1972**, *31,* 578.
(34) Thommes, M.; Köhn, R.; Fröba, M.*J. Phys. Chem. B* **2000**, *104*, 7932.
(35) Barrett, E. P.; Joyner, L. G.; Halenda, P. P. *J. Am. Chem. Soc.* **1951**, *73*, 373.
(36) Lastokie, C.; Gubbins, K. E.; Quirke, N. J. *J. Phys. Chem. B* **1993**, *97*, 4786.
(37) Ravikovitch, P. I.; Domhnaill, S. C. O.; Neimark, A.; Schüth, F.; Unger, K. K. *Langmuir* **1995**, *11*, 4765.
(38) Thommes, M.; Köhn, R.; Fröba, M.*Appl. Surf. Sci.* **2002**, *196*, 239.
(39) Köhn, R.; Fröba, M.*Catal. Today* **2001**, *68*, 227.

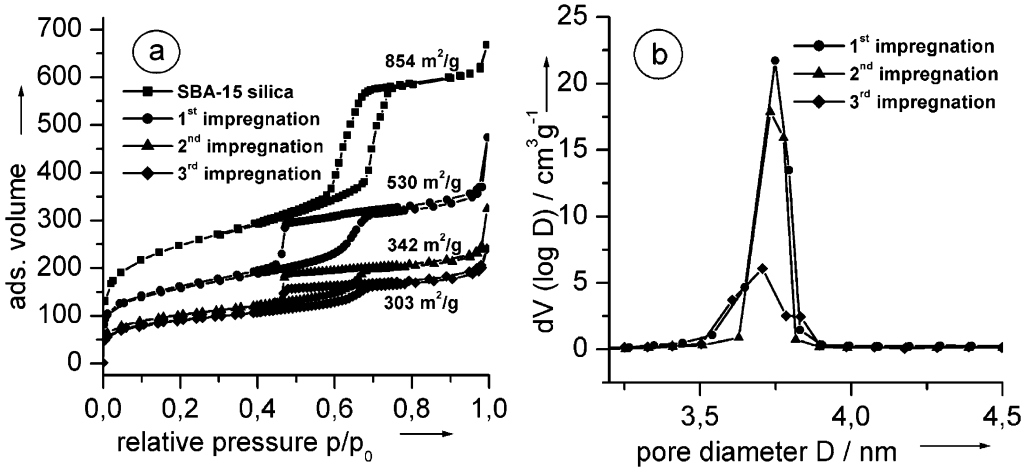

Figure 3. Nitrogen adsorption/desorption isotherms (a) and BJH pore-size distributions (b) of $Zn_{0.9}Mn_{0.1}S$@SBA-15 (6 nm).

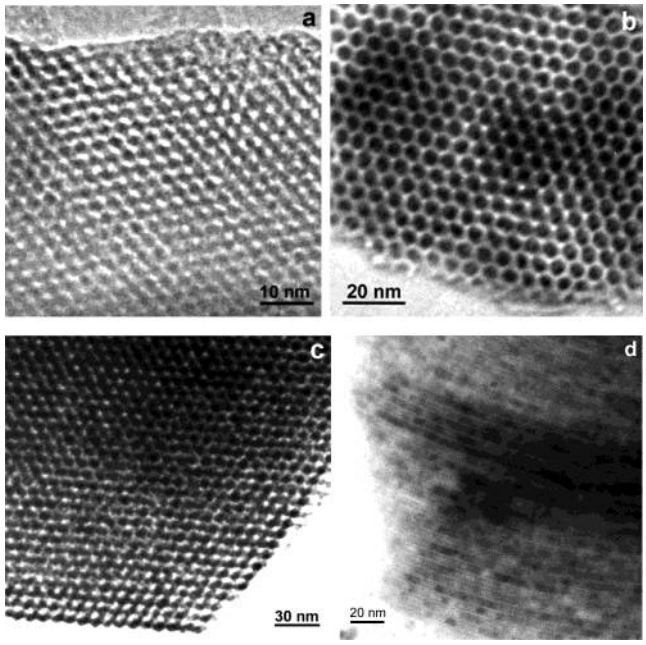

Figure 4. TEM images of (a) MCM-41 (3 nm pores), (b) SBA-15 (6 nm pores), (c) SBA-15 (9 nm pores), and (d) DMS compound/SBA-15 (6 nm pores) host/guest compound.

transmission electron microscopy (TEM). In Figure 4a−c the TEM images of the three pristine host structures are shown. The hexagonal ordering of the pores can clearly be seen. Figure 4d depicts a TEM image of a 6 nm host structure with an incorporated DMS compound. The view perpendicular to the pores reveals that the aligned pore channels are filled with the DMS compound. It can clearly be seen that still some single nanoparticles are present but they tend to agglomerate to denser wirelike structures. There is no evidence for larger particles being formed outside the pore system; i.e. the entire guest material is confined inside the channels of the porous host.

Infrared Spectroscopy. The infrared (IR) spectroscopy reveals the complete conversion of the incorporated acetates to the sulfides (Figure 5). Before the H_2S treatment the spectra look almost like a sum of MCM-41 silica and the bulk zinc−acetate spectra. After the H_2S/thermal treatment all bands corresponding to the acetate have vanished. Potentially formed acetic acid is removed by washing the samples with a certain amount of water for 30 min. Afterwards the resulting IR

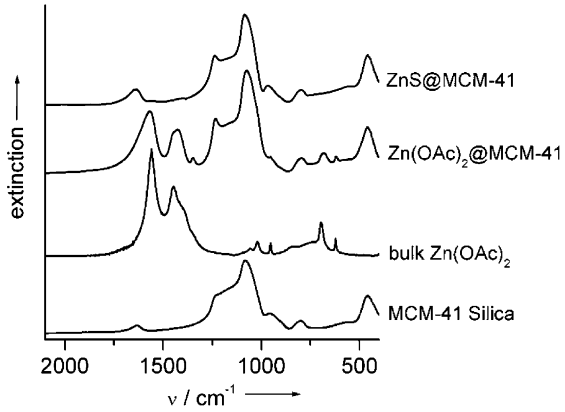

Figure 5. IR spectra taken at different steps of the synthesis of ZnS confined in MCM-41.

spectrum resembles that of the pristine MCM-41 material and it can be concluded that at this point only sulfides (which do not show IR activity) are present inside the pore systems.

Raman Spectroscopy. Parts a and b of Figure 6 depict Raman spectra in the vicinity of the LO phonon of bulk $Zn_{1-x}Mn_xS$ and $Zn_{1-x}Mn_xS$@SBA-15 (6 nm), respectively, with x ranging from 0.01 to 0.2. The Raman spectra of bulk $Zn_{1-x}Mn_xS$ are well-understood.[40] The feature at about 350 cm^{-1} corresponds to the LO phonon mode from the center of the Brillouin zone (reciprocal vector $q \approx 0$). This mode slightly shifts to lower frequencies, broadens with increasing Mn content x, and develops a shoulder on the low-frequency side. The LO phonon mode of ZnS transforms continuously into that of MnS; i.e. the $Zn_{1-x}Mn_xS$ alloy system shows a one-mode behavior. The only weak dependence of the LO phonon frequency on x is explained by the similarity of the LO phonon frequencies of ZnS and MnS. A value of 343 cm^{-1} has been determined for the LO phonon frequency of tetrahedrally coordinated MnS by IR reflectivity measurements.[41] It can be seen that with increasing x additional modes develop in the range between 310 and 330 cm^{-1}. These modes arise from the X- and L-points of the Brillouin zone, where the corresponding density of states is large, and become Raman-active by Mn substitution, which perturbs the translational symmetry. The Raman spectra of the

(40) Anatassiadou, A.; Liarokapis, E.; Anastassakis, E. *Solid State Commun.* **1989**, *69*, 137.
(41) Jahnke, E.; Goede, O.; Weinhold, V. *Phys. Status Solidi B* **1988**, *146*, K157.

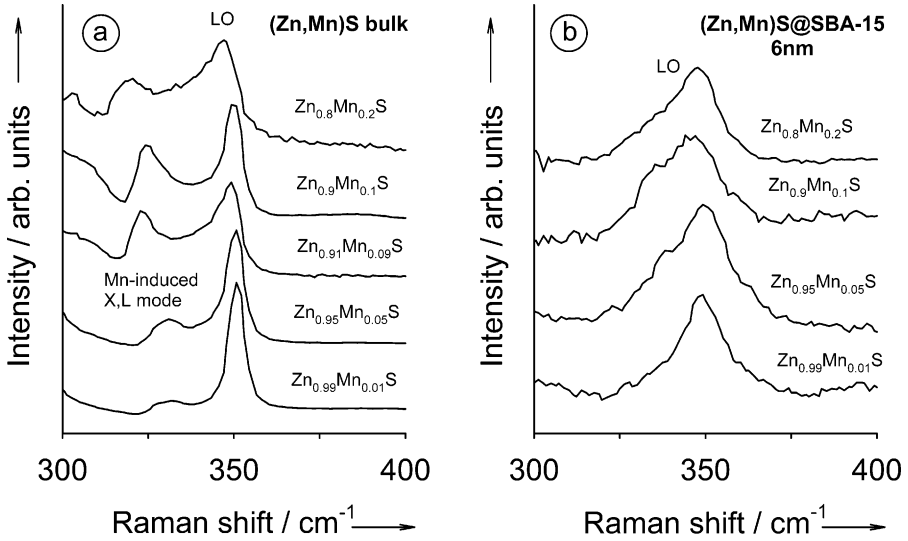

Figure 6. (a) Raman spectra of bulk $Zn_{1-x}Mn_xS$ of various x in the vicinity of the LO phonon. (b) Raman spectra of $Zn_{1-x}Mn_xS$@SBA-15 (6 nm) in the vicinity of the LO phonon. $T = 300$ K and laser excitation at 364 nm (3.41 eV).

$Zn_{1-x}Mn_xS$@SBA-15 (6 nm) also show clearly the LO phonon mode. The phonon mode is considerably broadened compared to the corresponding bulk modes but, with increasing x, also develops a shoulder on the low-frequency side. Furthermore, there is no indication of the Mn-induced X,L-modes at lower Raman shifts. The strong broadening of the LO phonon mode and the absence of the Mn-induced X,L-modes are due to the reduced dimensions of the nanoparticles. The reduction of the lateral dimensions should eventually lead to a breakdown of the concept of lattice periodicity and reciprocal space. The Mn-induced modes result from the density of states with high q-values which become ill-defined and thus unobservable when the concept of reciprocal space breaks down.

The reduction of the lateral dimensions of the semiconductor structure leads to phonon confinement. This results in an admixture of phonons with small nonzero q to the mode with $q = 0$.[42] This effect is a common characteristic of II−VI nanoparticles.[43−45] The admixture of modes of higher q usually leads to a red-shift of the peak position and to a broadening and concomitantly to a low-frequency wing of the LO phonon mode as its frequency usually decreases with increasing q. These features of phonon confinement are observable in Figure 7a. It shows the LO phonon spectra of bulk $Zn_{0.99}Mn_{0.01}S$, $Zn_{0.99}Mn_{0.01}S$@SBA-15 (6 nm), and $Zn_{0.99}Mn_{0.01}S$@MCM-41 (3 nm). The spectra of the $Zn_{0.99}Mn_{0.01}S$ nanoparticles are strongly red-shifted and broadened with respect to the bulk reference. As expected, both effects are more significant for $Zn_{0.99}Mn_{0.01}S$@MCM-41 (3 nm) than for $Zn_{0.99}Mn_{0.01}S$@SBA-15 (6 nm).

The confined-phonon model introduced by Campbell and Fauchet yields different results for wire-like cylindrical and spherical nanoparticles.[42] The model assumes that the $q = 0$ phonon can be described by the lattice-periodic part of bulk material $u(q=0,r)$ multiplied by an envelope function $\Psi_s(q=0,r)$. The envelope function is determined by the shape and the dimensions of the nanoparticle. The corresponding line shape of the LO phonon in a nanoparticle is given by

$$I(\omega) \cong \int_{\text{1st Brillouin zone}} \mathrm{d}^3q \frac{|C(0,q)|^2}{(\omega_0 - \omega(q))^2 + (\Gamma_0/2)^2} \quad (1)$$

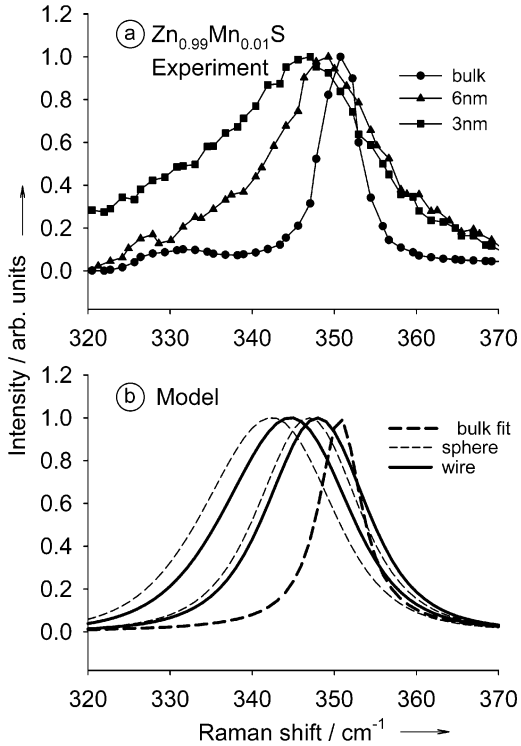

Figure 7. (a) Raman spectra in the vicinity of the LO phonon of bulk $Zn_{0.99}Mn_{0.01}S$, $Zn_{0.99}Mn_{0.01}S$@SBA-15 (6 nm), and $Zn_{0.99}Mn_{0.01}S$@MCM-41 (3 nm). $T = 300$ K and laser excitation at 364 nm (3.41 eV). (b) Lorentzian fit of the LO phonon of bulk $Zn_{0.99}Mn_{0.01}S$. Calculated LO phonon line shapes for spherical $Zn_{0.99}Mn_{0.01}S$ nanoparticles and cylindrical $Zn_{0.99}Mn_{0.01}S$ wires with diameters of 3 and 6 nm.

where ω_0 is the frequency of the LO phonon at $q = 0$; $\omega(q)$ is the (spherical) bulk LO phonon dispersion; and Γ_0 is the full width at half-maximum of the bulk LO phonon (Lorentzian) line shape. $C(0,q)$ are the Fourier coefficients of the envelope

(42) Campbell, I. H.; Fauchet, P. M. *Solid State Commun.* **1986**, *58*, 739.
(43) Verma, P.; Gupta, L.; Abbi, S. C.; Jain, K. P. *J. Appl. Phys.* **2000**, *88*, 4109.
(44) Rajalakshmi, M.; Arora, A. K.; Bendre, B. S.; Mahamuni, S. *J. Appl. Phys.* **2000**, *87*, 2445.
(45) Curri, M. L.; Agostiano, A.; Manna, L.; Della Monica, M.; Catalano, M.; Chiavarone, L.; Spagnolo, V.; Lugará, M. *J. Phys. Chem. B* **2000**, *104*, 8391.

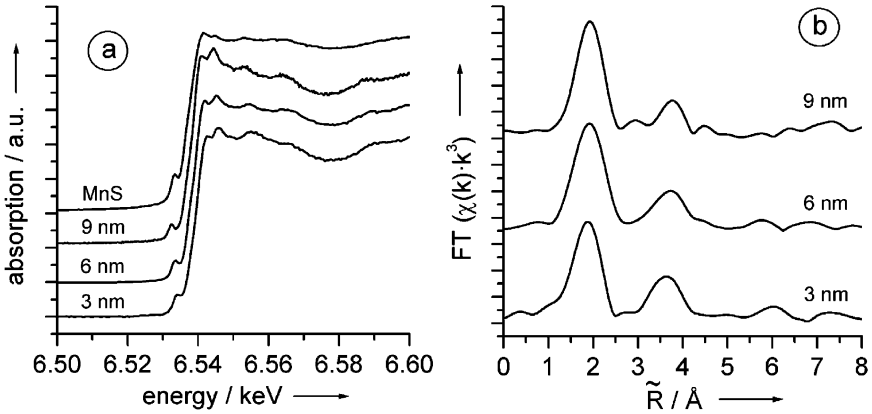

Figure 8. (a) Normalized Mn K-XANES spectra of $Zn_{0.7}Mn_{0.3}S$ confined in 3, 6, and 9 nm pores and bulk MnS (wurzite structure). (b) Modified radial distribution functions (m-RDF, not phase-shift corrected) of the Mn K-EXAFS spectra of $Zn_{0.7}Mn_{0.3}S$ confined in 3, 6, and 9 nm pores.

function $\Psi(q=0,r)$. Campbell and Fauchet give the following expressions for a sphere and a cylindrical wire of infinite length:

$$|C_{\text{sphere}}(0,q)|^2 \cong \exp\left(-\frac{q^2 d_{\text{sphere}}^2}{16\pi^2}\right)$$

$$|C_{\text{wire}}(0,q_\perp, q_z)|^2 \cong \exp\left(-\frac{q_\perp^2 d_{\text{wire}}^2}{16\pi^2}\right)\delta(q_z) \qquad (2)$$

where d_{sphere} and d_{wire} are the diameters of the sphere and the wire, respectively. $q_\perp$ and q_z are the q-vectors perpendicular and parallel to the wire axis. Using the $d^3q = 4\pi q^2\, dq$ for the sphere and $d^3q = 2\pi q_\perp\, dq_\perp\, dq_z$ for the infinite wire allows one to calculate the LO phonon line shape for wire-like and spherical nanoparticles of different diameters using eq 1.

We employed the model to analyze the line shapes of $Zn_{0.99}Mn_{0.01}S$ nanoparticles shown in Figure 7a. For the phonon-dispersion $\omega(q)$ we used that along the Δ-direction of the Brillouin zone of zincblende ZnS bulk.[46] To determine Γ_0, we fitted the LO phonon spectrum of bulk $Zn_{0.99}Mn_{0.01}S$ (Figure 7a) by a Lorentzian line shape. The fit (Figure 7b) yielded $\Gamma_0 \approx 6\ \text{cm}^{-1}$. However, the line widths of the confined-phonon line shapes calculated using these parameters were too narrow compared to the experimental results. A better agreement was obtained by using $\Gamma_0 \approx 20\ \text{cm}^{-1}$. It is well-known that the line widths of the bulk LO phonon is very sensitive to the degree of crystallinity of the material and that the degree of crystallinity itself usually increases with increasing synthesis temperature. Thus, the larger Γ_0 for the $Zn_{0.99}Mn_{0.01}S$ nanostructures reflects simply the differences in the synthesis of the nanostructures and the bulk reference samples used in the Raman experiments. The latter were synthesized at much higher temperatures (about 1000 °C) using Bridgman techniques. The synthesis temperature of the nanostructures was considerably lower to minimize diffusion of the Mn to the surface, which, in contrast to bulk-material synthesis, is a severe problem in the synthesis of nanostructures because of their larger surface-to-volume ratio. It is worth noting that the red-shift of the maximum of the confined-phonon line shape with respect to ω_0 as a function of the diameter exhibits only a weak dependence on Γ_0 for both wires and spheres. Figure 7b depicts LO phonon line shapes for spherical $Zn_{0.99}Mn_{0.01}S$ nanoparticles and cylindrical $Zn_{0.99}Mn_{0.01}S$ wires with diameters of 3 and 6 nm calculated using $\Gamma_0 = 20\ \text{cm}^{-1}$. It demonstrates that with respect to ω_0 the red-shift of the maximum of the confined-phonon line shape is smaller for wires than for spheres of the same diameter. The red-shifts observed in the experiment show a better agreement with those calculated for wire-shaped nanostructures of the same nominal diameter. The red-shifts calculated for spherical particles are too large. This can be tentatively interpreted as a sign that the average (Zn,Mn)S nanoparticles incorporated into the SiO_2 pores have an elongated shape with lateral extensions close to the pore diameter and extensions along the pore axis larger than the pore diameter; i.e. the average (Zn,Mn)S nanoparticles are wire-like.

X-ray Absorption Spectroscopy. X-ray absorption spectroscopy is the method of choice to distinguish whether the pore system contains the two binary sulfides, ZnS and MnS, or the ternary (II,Mn)VI compound, $Zn_{1-x}Mn_xS$, with the Mn^{2+} ions distributed randomly inside the ZnS matrix. Zn K-edge measurements (not shown) proved the existence of ZnS particles inside the respective pore systems. To investigate the local structure around the Mn^{2+} ions, X-ray absorption spectroscopy at the Mn K-edge was carried out as well. Figure 8a displays the normalized X-ray absorption near-edge structure (XANES) regions of the Mn K-edge spectra of $Zn_{0.7}Mn_{0.3}S$ confined in 3, 6, and 9 nm pores. The XANES region of the spectra can be used as a "fingerprint" of the respective material. It can clearly be seen, that exactly the same features in the XANES region of the MnS reference (wurtzite structure) cannot be found in the spectra of manganese-doped ZnS. Hence, Mn^{2+} is not located inside a MnS matrix, but manganese is present in the samples.

Figure 8b shows the not phase-shift corrected modified radial distribution functions (m-RDF) of $Zn_{0.7}Mn_{0.3}S$ confined inside 3, 6, and 9 nm pores; in Table 1 the fit results are summarized. The first Mn−S shell is slightly shifted to smaller distances for all incorporated samples. This is due to the fact that the distance between manganese and sulfur in pure MnS is significantly larger (2.42 Å for the wurtzite structure) than the Zn−S distance in ZnS (2.34 Å for wurtzite). The Mn−S distance in the investigated samples lies between these two values but is very similar to the expected bond length in pure MnS. Thus, replacing Zn^{2+} by Mn^{2+} in ZnS results in a locally slightly distorted "MnS" geometry.

(46) *Landolt-Börnstein−Numerical Data and Functional Relationships in Science and Technology*, Vol. 17b; Madelung, O., Schulz, M., Weiss, H., Eds.; Springer, Berlin−Heidelberg−New York, 1982.

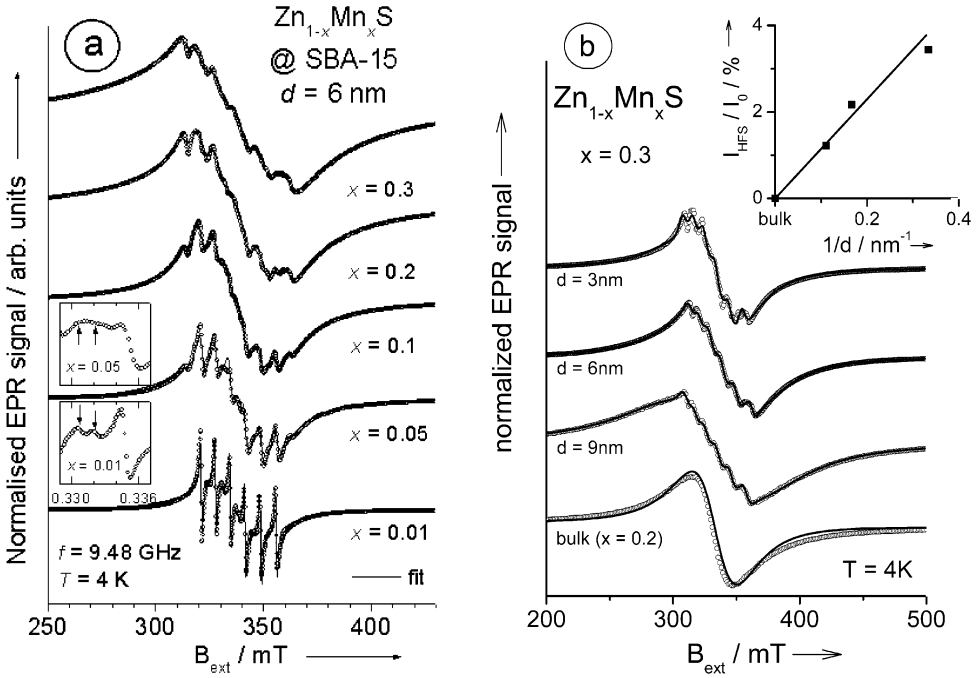

Figure 9. (a) Normalized EPR spectra of $Zn_{1-x}Mn_xS$@SBA-15 (6 nm) for different values for x. The fit curves consist of the field derivative of the sum of one broad Lorentz curve and one (for $x = 0.01$ and 0.3) or two hyperfine structures (for $x = 0.05$, 0.1, and 0.2) of six Lorentz curves. Insets: hyperfine transitions on an enlarged field scale for $x = 0.01$ (lower) and $x = 0.05$ (upper), the arrows indicate the positions of the forbidden transitions. (b) Normalized EPR spectra of bulk $Zn_{0.8}Mn_{0.2}S$ and nanostructured $Zn_{0.7}Mn_{0.3}S$ in MCM-41 ($d = 3$ nm), SBA-15 ($d = 6$ nm), and SBA-15 ($d = 9$ nm). The fit curves have been calculated as in a. Inset: Plot of intensity ratio I_{HFS}/I_0 between hyperfine structure and full spectrum as a function of the inverse pore diameter $1/d$.

Table 1. Fit Results of the Mn K-EXAFS Measurements[a]

sample	N	R (Å)	$\Delta\sigma^2$ ($\cdot 10^{-3}$ Å^2)
$Zn_{0.7}Mn_{0.3}S$@MCM-41 (3 nm)	4.00	2.38	6.0
	11.10	3.95	17.1
$Zn_{0.7}Mn_{0.3}S$@SBA-15 (6 nm)	4.00	2.41	8.3
	11.40	3.98	16.6
$Zn_{0.7}Mn_{0.3}S$@SBA-15 (9 nm)	4.00	2.41	6.6
	10.24	3.98	16.9

[a] Abbreviations: N = coordination number; R = bond length; $\Delta\sigma^2$ = Debye−Waller factor. The amplitude reduction factor S_0^2 was extracted from MnS with manganese in octahedral coordination geometry (rock-salt structure).

For the incorporated diluted magnetic semiconductors $Zn_{0.7}Mn_{0.3}S$ the next-nearest-neighbor distance (Mn−Zn) is within a minor deviation, again nearly the same as in pure bulk MnS. The corresponding Mn−Mn distance would be 3.96 Å, and good agreement can be observed for all samples. The associated coordination numbers are only slightly smaller than in MnS. Again, these effects can be explained by a small local disorder in the ZnS matrix arising from the substitution of Zn by Mn leading to a distorted Mn−S geometry. From these results it can be concluded that the amount of manganese ions aggregated at the surface of the nanoparticles is very small, Mn^{2+} ions really substitute Zn^{2+} in the nanocrystalline structure, and a $Zn_{1-x}Mn_xS$ nanocrystal is formed.

However, it is not possible to distinguish whether the $Zn_{1-x}Mn_xS$ nanocrystals are of wurtzite or zincblende structure. Both crystal structures are very similar and differ slightly only in the second coordination sphere. For example the Zn−Zn distance in bulk ZnS is 3.78 Å for zincblende and 3.82 Å for wurtzite. For bulk $Zn_{1-x}Mn_xS$ the crystal structure is known to be zincblende for $x < 0.1$ and wurtzite for $0.1 < x < 0.45$. With the passage from bulk to nanocrystals the crystal structure changes though.[47,48] We have reported on manganese-doped CdS nanoclusters confined in mesoporous silica matrices with both zincblende and wurtzite structure.[22,24]

Electron Paramagnetic Resonance Measurements. The electron paramagnetic resonance (EPR) spectra of the incorporated DMS compounds are very similar for all three host structures. In Figure 9a five $Zn_{1-x}Mn_xS$@SBA-15 (6 nm) samples with $x = 0.01$, 0.05, 0.1, 0.2, and 0.3 are shown. All spectra were taken at 4 K and were normalized to the same amplitude. The spectra are typical for exchange-coupled Mn^{2+} ions within a II/VI semiconductor compound[49−51] and can best be explained for low x. The spectra basically consist of a sextet of sharp lines. This sextet, which is centered at a g-value of $g = 1.999$, is associated with the allowed ($\Delta m_S = \pm 1$; $\Delta m_I = 0$) magnetic dipolar transitions between the hyperfine-split Zeeman levels of the $^6S_{5/2}$ (or $^6A_1$) ground state of the Mn^{2+} 3d-electrons. The hyperfine structure arises from the interaction between the $S = 5/2$ spin of the unpaired 3d-electrons with the $I = 5/2$ spin of the ^{55}Mn nucleus. The hyperfine splitting characteristic for Mn^{2+} in ZnS amounts to about $\delta B_{HFS} = 7.0$ mT between neighboring allowed transitions in zincblende as well as in wurtzite structure.[10] The splitting observed in the spectrum of the sample with 1% Mn agrees well with this value.

With increasing Mn content the dipolar interaction and exchange coupling merge the hyperfine structure into one broad resonance line, which is documented best for $x = 0.3$. But this broad line can already be identified for $x = 0.01$. The spectrum for $x = 0.01$ is satisfactorily described by the sum of the broad line and the hyperfine structure of six lines. Both the broad line and the hyperfine lines were assumed to be of Lorentzian shape.

(47) Cizeron, J.; Pileni, M. P. *J. Phys. Chem. B* **1995**, *99*, 17410.
(48) Vogel, W.; Urban, J.; Kundu, M.; Kulkarni, S. K. *Langmuir* **1997**, *13*, 827.
(49) Schneider, J.; Sircar, S. R.; Rüber, A. *Z. Naturforsch. A* **1963**, *18*, 980.
(50) Lambe, J.; Kikuchi, C. *Phys. Rev.* **1960**, *119*, 1256.
(51) Ishikawa, Y. *J. Phys. Soc. Jpn.* **1966**, *21*, 1473.

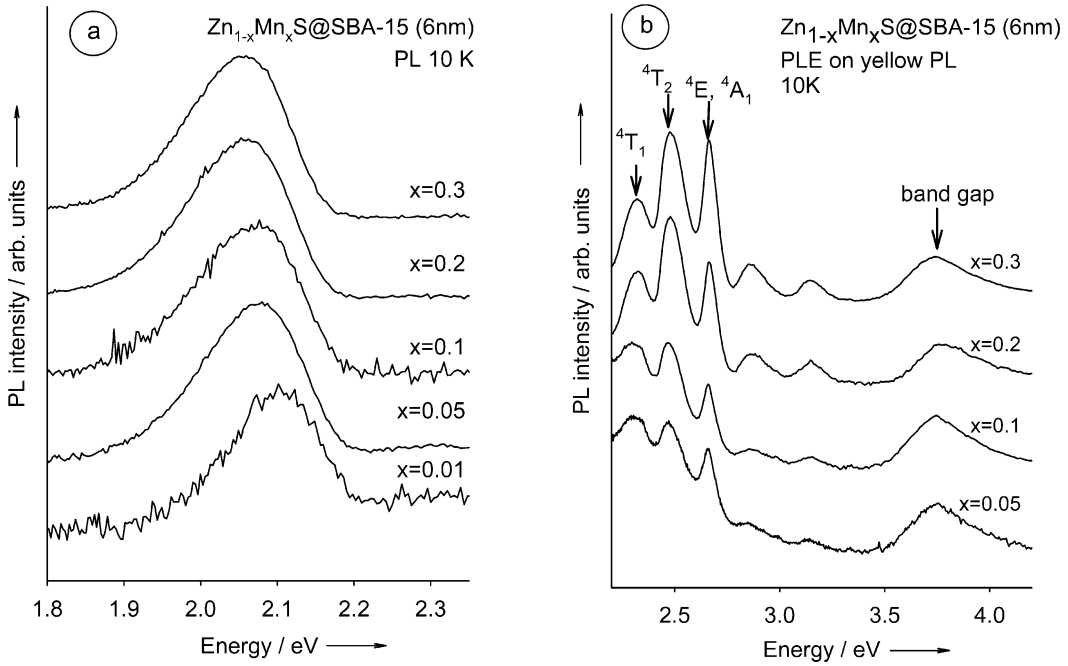

Figure 10. (a) PL spectra of $Zn_{1-x}Mn_xS$@SBA-15 (6 nm) for various x. (b) Corresponding PLE spectra for $x \geq 5\%$ detected at 600 nm. $T = 10$ K.

In addition it was necessary to take into account a slight linear increase of the hyperfine splitting with the external field due to second-order contributions.

A close inspection of Figure 9a reveals that at low Mn concentration each hyperfine line exhibits a pair of satellites at lower external magnetic field associated with the forbidden ($\Delta m_S = \pm 1$; $\Delta m_I = \pm 1$) hyperfine transitions (see lower inset of Figure 9a). The forbidden hyperfine transitions in the spectra with the lowest manganese content ($x = 0.01$) are typical for Mn^{2+} ions in the tetrahedral environment of a Zn-site in a zincblende crystal. In the case of a wurtzite crystal these lines are much more prominent[52] and are merging with the lines of the allowed hyperfine transitions, as it is observed for samples with larger amounts of manganese ($x \geq 0.05$; see upper inset of Figure 9a). Thus, it can be concluded that the crystal structure of the incorporated (II,Mn)VI semiconductors is zincblende only for $x = 0.01$, whereas higher doping levels with Mn^{2+} result in a wurtzite structure.

At the same time it has to be noticed that with increasing x an additional hyperfine structure of six lines with a larger splitting of about $\delta B_{HFS} = 9.5$ mT evolves and persists even at 30% Mn content. This hyperfine structure may result from isolated Mn^{2+} ions on the surface or interstitial places of the $Zn_{1-x}Mn_xS$ nanowires.[10]

To clarify this, we compared the spectra of $Zn_{0.7}Mn_{0.3}S$ nanostructures with different pore sizes, as shown in Figure 9b. All spectra were taken at 4 K, where the hyperfine structure can be best identified in the nanowires, because with increasing temperature it becomes more and more smeared out. In the bulk sample $Zn_{0.8}Mn_{0.2}S$, which was used for comparison, no hyperfine structure was visible at all. The spectra were again fitted by the sum of one broad Lorentz curve and a hyperfine structure of six Lorentz curves. All spectra could be satisfactorily described in this way. The intensity, which is proportional to the spin susceptibility and hence to the number of spins, corresponds to the area below the absorption curve. It is given by the 2-fold field integration of the EPR signal, which itself represents the field derivative of the absorption. The fit allows one to separate the intensity of the hyperfine structure I_{HFS} from the intensity of the full spectrum I_0 and hence to determine the relative number of Mn^{2+} ions, which give rise to the hyperfine structure. The inset of Figure 9b exhibits a linear dependence of the intensity ratio I_{HFS}/I_0 on the inverse pore diameter $1/d$. This corroborates the assumption that the hyperfine structure arises from manganese spins on the surface of the nanowires instead of interstitial positions, because the surface-to-volume ratio also varies with $1/d$. For the bulk sample this is by far smaller than for the nanowires, and therefore the hyperfine structure vanishes. The absolute value of the intensity ratio is only about 20% of the value, which one would expect for the full surface layer of approximately 0.3 nm thickness; i.e., only 20% of the Mn ions at the surface are bound weakly enough to give rise to the hyperfine structure. From the EPR results we can deduce that the majority of the Mn^{2+} ions is well-incorporated into the $Zn_{1-x}Mn_xS$ nanowires and only a small amount remains weakly bound at their surface. This amount of aggregated Mn ions at the surface of the nanoclusters corresponds to less than 4, 2, and 1% of the total Mn-content for the 3, 6, and 9 nm wires, respectively.

Photoluminescence and Photoluminescence Excitation Measurements. Parts a and b of Figure 10 depict the photoluminescence (PL) spectra and the corresponding photoluminescence excitation (PLE) spectra of $Zn_{1-x}Mn_xS$@SBA-15 (6 nm) for different x. The PL spectra of all samples with $x > 0.01$ consist basically of one emission band at about 600 nm. This so-called yellow PL band originates from the $^4T_1$ to $^6A_1$ transition within the $3d^5$ shell of Mn^{2+} on a cation site with tetrahedral symmetry. It is a common feature in wide-gap manganese-doped II−VI semiconductors.[53−55] No band-gap-

(52) Hofmann, D. M.; Hofstaetter, A.; Leib, U.; Meyer, B. K.; Counio, C. *J. Cryst. Growth* **1998**, *184−185*, 383.

(53) Goede, O.; Heimbrodt, W. *Phys. Status Solidi B* **1988**, *146*, 11.

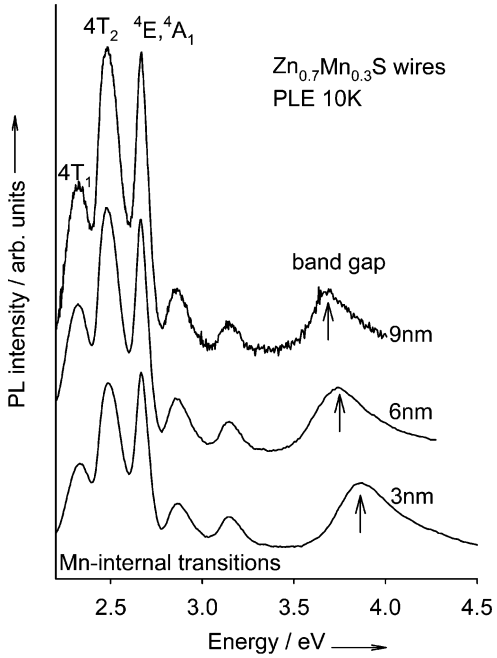

Figure 11. PLE spectra of $Zn_{0.7}Mn_{0.3}S$ wires of diameters of 3, 6, and 9 nm.

related excitonic PL is observable due to the efficient energy transfer from the $Zn_{1-x}Mn_xS$ band states into the Mn^{2+} subsystem. The PLE spectra show a distinct series of peaks. The direct absorption of the Mn^{2+} $3d^5$ shell causes the signals at lower energies. They correspond to transitions from the $^6A_1$ ground state to the higher excited states $^4T_1$, $^4T_2$ and ^4E, $^4A_1$. This confirms, that the Mn^{2+} ions are incorporated on the tetrahedrally coordinated Zn sites of the ZnS lattice, forming the $Zn_{1-x}Mn_xS$ semiconductor. Assuming that excitonic recombination processes and the energy transfer into the Mn system only show a weak dependence on x, the increase in intensity of the internal transitions with respect to the band-gap-related feature reflects the increase of the direct absorption of the 3d shell of Mn^{2+} with increasing x. It confirms that most of the Mn ions are incorporated into the $Zn_{1-x}Mn_xS$, i.e., that there is no significant Mn diffusion to the surface. The transition energies of the Mn internal transitions are approximately independent of x up to $x = 0.3$.

The broader excitation band at the highest energies is the band-to-band transition of the wires. This signal is only observed because of the efficient energy transfer from the band states into the Mn^{2+} $3d^5$ shell. The band gap shows quantum confinement but only a weak dependence on Mn concentration. This is due to the fact that the band gaps of bulk ZnS and MnS are very similar, 3.78 and 3.7 eV, respectively.[56,57]

The PL and PLE spectra of the $Zn_{1-x}Mn_xS$ wire samples of 3 and 9 nm are very similar to those in Figure 10. As an example Figure 11 depicts PLE spectra of $Zn_{0.7}Mn_{0.3}S$ wires of different diameters. The band-gap-related signal shifts significantly to higher energies due to increased quantum confinement. Figure 12a summarizes the variation of the band-gap energy with x and the wire diameter, extracted from the PLE spectra taken at 10 K. It can clearly be seen that confinement effects increase with decreasing wire diameter. The confinement energy is about 150 meV for the 3 nm wires. This is significantly smaller than for $Cd_{1-x}Mn_xS$ or $Cd_{1-x}Mn_xSe$ wires with similar diameters, where the confinement energy was reported to be 400 or 200 meV, respectively.[21] Going from $Cd_{1-x}Mn_xSe$ to $Cd_{1-x}Mn_xS$ to $Zn_{1-x}Mn_xS$ the band-gap difference between the manganese-doped II−VI semiconductor and SiO_2 as well as the exciton Bohr radius is decreasing. The energies of the band-to-band transition of the 9 nm wires are close to the corresponding bulk values; i.e., confinement effects are very small.

Figure 11 shows that the intensity of the Mn internal transition with respect to the intensity of the band-gap-related feature decreases with decreasing wire diameter. The intensity ratio scales roughly with the ratio of the volume of the surface monolayer to the total volume, suggesting that the effect is related to the nanostructuring. However, it cannot be analyzed quantitatively on the basis of the continuous wave (cw) PL measurements as the change of intensity ratio also reflects the changes of the dynamics of the luminescence process. Nonradiative recombination, radiative recombination of the excitons, and the energy transfer from the excitons into the Mn system will all depend strongly on the nanostructuring, much stronger than their dependence on x for a fixed nanostructure size. Time-resolved PL measurements are required to explain the observed behavior in more detail.

It can also be seen in Figure 11 that the Mn^{2+} $3d^5$ internal transitions of the 3, 6, and 9 nm samples are very similar. The energy positions of the Mn internal transitions depend strongly on the crystal field of the Mn site which can be analyzed using the Tanabe−Sugano model[58] as a function of the crystal-field parameter Dq. We used the Racah parameters $B = 50$ meV and $C = 434$ meV. In Figure 12b the calculated energies of the excited states of a Mn^{2+} $3d^5$ ion in a T_d symmetric ligand field are depicted as a function of Dq. Comparing the calculated energy positions with the experimentally observed positions allows one to deduce the crystal-field parameter Dq. For the 3 and 6 nm $Zn_{1-x}Mn_xS$ wires the best agreement is obtained for $Dq = 0.64$ and in the case of the 9 nm wires for $Dq = 0.65$. For bulk $Zn_{0.9}Mn_{0.1}S$ we obtained $Dq = 0.64$. Because Dq is indirectly proportional to the fifth power of the anion−cation distance, it can be concluded that the Mn−S bond length in all $Zn_{1-x}Mn_xS$ wires is comparable to that of bulk $Zn_{1-x}Mn_xS$ within about ±1%. The good agreement between experiment and theory also confirms that the majority of the Mn ions in the wires are tetrahedrally coordinated.

Conclusions

The results of the various applied techniques confirm that high-quality $Zn_{1-x}Mn_xS$ wires with x ranging from 0.01 to 0.3 have been formed and stabilized inside highly ordered pore systems of hexagonally ordered silica matrices. P-XRD and physisorption measurements as well as TEM investigations show that the formation of the ternary sulfide takes places preferentially inside the pore system of the mesoporous host structures. A careful TEM analysis shows that the lateral size of the $Zn_{1-x}Mn_xS$ nanoparticles is limited by the pore diameter and that the nanoparticles tend to agglomerate to denser wire-like structures.

(54) Goede, O.; Heimbrodt, W.; Weinhold, V. *Phys. Status Solidi B* **1986**, *136*, K49.
(55) Heimbrodt, W.; Benecke, C.; Goede, O.; Gumlich, H.-E. *Phys. Status Solidi B* **1989**, *154*, 405.
(56) Theis, D. *Phys. Status Solidi B* **1967**, *79*, 125.
(57) Goede, O.; Heimbrodt, W.; Lamla, M.; Weinhold, V. *Phys. Status Solidi B* **1989**, *146*, K65.
(58) Tanabe, Y.; Sugano, S. *J. Phys. Soc. Jpn.* **1954**, *9*, 753.

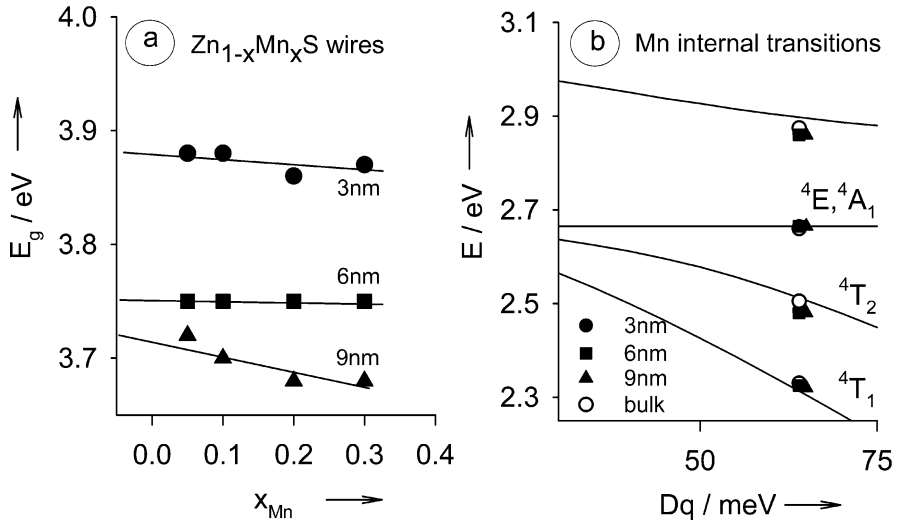

Figure 12. (a) Comparison of the band-gap variation with x for $Zn_{1-x}Mn_xS$ wires of 3, 6, and 9 nm at $T = 10$ K. The corresponding solid lines are guides to the eye. (b) Energies of the internal transitions of Mn^{2+} ions in a T_d symmetric crystal field versus the field parameter Dq using the Racah parameters $B = 50$ meV and $C = 434$ meV, calculated in the framework of the Tanabe−Sugano model (solid lines). Experimental points for $Zn_{0.9}Mn_{0.1}S$ bulk and $Zn_{0.7}Mn_{0.3}S$ wires of 3, 6, and 9 nm.

The local environment of the Mn^{2+} ions was probed by X-ray absorption spectroscopy, EPR, and PLE experiments. These reveal that the Mn^{2+} ions randomly substitute Zn^{2+} ions inside the ZnS crystal structure. Furthermore, the analysis of the EPR results suggests that the amount of Mn^{2+} ions aggregated at the surface of the nanostructures due to diffusion is very small, i.e., most of the Mn ions are incorporated to form $Zn_{1-x}Mn_xS$. The amount of Mn at the surface corresponds to less than 4, 2, and 1% of the total Mn content for the 3, 6, and 9 nm wires, respectively, even for $x = 0.3$.

PLE and Raman measurements show the strong effect of the reduced dimensions on the vibrational and electronic properties of $Zn_{1-x}Mn_xS$. Clear trends as a function of wire diameter are observable for the confined phonons as well as for the confined excitons. The quantum-confinement effect of the excitons leads to an increase of the observed band gap with decreasing diameter in the $Zn_{1-x}Mn_xS$ wires. Typical phonon-confinement effects such as the red-shift of the position and the asymmetric broadening of the LO phonon line with decreasing nanostructure size are observed. An analysis of the LO phonon line shapes corroborates that wire-like $Zn_{1-x}Mn_xS$ nanostructures are formed.

High-quality DMS nanostructures such as the $Zn_{1-x}Mn_xS$ wires of well-defined diameters presented here will prove useful in future studies of magnetic, electronic, and vibrational phenomena at low dimensions. The understanding of magnetism at low dimensions is an essential requirement for a further miniaturization of electronic and spintronic devices.

Experimental Section

Synthesis of the Pristine Mesoporous MCM-41 Silica. For the synthesis of the pristine MCM-41 silica 0.25 mol of hexadecyltrimethylammonium bromide (C_{16}TABr, Merck) were dissolved in 35 mol of water by stirring and heating to 65 °C. A 0.2 mol amount of tetramethylammonium hydroxide (TMAOH, 25% in water, Merck) and, under vigorous stirring, 1 mol of SiO_2 (Cab−O−Sil, Riedel-de-Haen) were added. The mixture was kept stirring at 65 °C for 30 min, transferred into a Teflon-lined steel autoclave, and stored at room temperature for 24 h. The autoclave was then statically heated to 150 °C for 24 h. The resultant white precipitate was filtered and washed several times with warm deionized water. Drying at room temperature under vacuum gave a white powder which was stored at 120 °C for 24 h. Calcination was carried out statically at 550 °C for 24 h (heating rate: 1°/min).

Synthesis of Pristine Mesoporous SBA-15 Silica. For the synthesis of SBA-15 silica 0.8 g of Pluronic P-123 were dissolved in 24 g of water and 2.86 g of concentrated hydrochloric acid at 30 °C on a waterbath. After the addition of 1.6 g of tetraethyl orthosilicate (TEOS) the reaction mixture was stirred for 24 h at 30 °C. The resulting gel was transferred into a Teflon-lined steel autoclave and heated to 80 °C for 24 h to obtain 6 nm pores and 140 °C for 24 h to obtain 9 nm pores. The resulting white powder was washed three times with deionized water, and the surfactant was removed by Soxleth extraction at 120 °C with a mixture of 97 mL of ethanol and 3 mL of concentrated hydrochloric acid.

Synthesis of the DMS/Mesoporous Silica Host/Guest Material. The impregnation procedure was carried out by stirring 0.5 g of the porous host material (MCM-41 or SBA-15) in a 0.5 M solution of zinc acetate (Merck) and manganese acetate (Merck) with the desired ratio of Zn/Mn for 10 min. No further tuning on the pH value was carried out. The dispersion was separated by centrifugation. The residue was dried under vacuum and stored in a H_2S atmosphere at 100 °C for 24 h. The impregnation/conversion cycle was carried out twice for MCM-41 as the host structure and three times for SBA-15. After the complete impregnation/conversion cycle the sample was washed free of the remaining acetate by stirring in 20 mL of deionized water for 30 min.

Analyses and Measurements. Powder X-ray diffraction patterns were recorded at room temperature with a Bruker AXS D8 Advance diffractometer (Cu Kα) in θ/θ geometry with a secondary monochromator.

Physisorption measurements were carried out using a Quantachrome Autosorb 6 instrument with nitrogen as adsorptive at 77 K. The BET surface areas were calculated from $p/p_0 = 0.03-0.3$ in the adsorption branch; the BJH pore size distributions were calculated from the desorption branch. Before each sorption measurement the sample was outgassed at 120 °C for at least 24 h under turbomolecular pump vacuum.

Infrared spectroscopy was carried out using a Perkin-Elmer FT-IR 1720 in the range from 400 to 4000 cm^{-1} in shuttle mode.

Phonon Raman spectra were obtained at room temperature. An argon-ion laser (Coherent Innova Sabre) operating single line at 364 nm (3.41 eV) with an output power of about 100 mW was used

for excitation. A triple Raman spectrometer was used for light dispersion and detection. It consisted of a subtractive double stage (ISA 1680B) employed as band-pass and a 1.25 m monochromator stage (Spex 1250m) equipped with a nitrogen-cooled CCD (ISA Spectrum One) for detection.

The transmission electron micrographs were recorded on a Philips CM 300 UT and on a Philips CM 30 ST.

The XAFS measurements of the Mn K-edges were recorded at HASYLAB at DESY on the beamline A1. All data were taken at room temperature with a silicon (111) monochromator in fluorescence mode. For data analyses the programs FEFF 7.01[59] and WinXAS[60] were used.

The photoluminescence-based optical measurements were carried out at 10 K with the specimen mounted in a contact-gas He-cryostat (Cryovac K 1104 C). Tuneable monochromatic excitation light with a bandwidth of 5 nm was provided either by a tungsten lamp (for PLE measurements) or by a xenon lamp (for PL measurements) followed by a 0.32 m monochromator (ISA Triax 320). The sample luminescence was detected using a 0.5 m spectrometer (Zeiss) with a resolution better than 1 nm equipped with a GaAs photomultiplier (Hamamatsu). For the PL measurements the sample was excited either with the 325 nm light (3.81 eV) of a HeCd laser (Kimmon IK series) or the lamp system set to 470 nm (2.63 eV). The PL signal was detected in the range from 500 to 700 nm. For the PLE measurements the PL intensity was detected at 600 nm varying the wavelength of the excitation light from 270 to 580 nm.

Electron paramagnetic resonance measurements were performed using a Bruker Elexsys 500 CW spectrometer at X-band frequencies (9.48 GHz) and magnetic fields up to 1 T at temperatures between 4 and 200 K in a continuous-flow He cryostat. As the signal-to-noise ratio is improved by a lock-in technique with field modulation, the EPR spectra represent the field derivative of the microwave power absorbed by the sample from the transverse magnetic microwave field as a function of the external static magnetic field.

Acknowledgment. The authors would like to thank Günter Koch (Institute of Inorganic and Analytical Chemistry, Justus-Liebig University Giessen) for the transmission electron micrographs. Financial support by the Deutsche Forschungsgemeinschaft (Grants Fr 1372/4-2, 4-3 and He 2298/4-2, 4-3) and the Fonds der Chemischen Industrie is gratefully acknowledged. This work was partially supported by the Bundesministerium für Bildung und Forschung (BMBF) under Contract No. 13N6917/0 (EKM) and by the Optodynamics Center of the Philipps University.

(59) Rehr, J. J.; Mustre de Leon, J.; Zabinsky, S. I.; Albers, R. C. *J. Am. Chem. Soc.* **1991**, *113*, 5135.
(60) Ressler, T. *J. Synchrotron Radiat.* **1998**, *5*, 118.